



HAL
open science

RayActive: An all-in-one R2S neutron induced activation analysis tool based on new intrinsic resolution methods

N. Dray, Eric Suraud, C. Dossat, N. Chatry

► **To cite this version:**

N. Dray, Eric Suraud, C. Dossat, N. Chatry. RayActive: An all-in-one R2S neutron induced activation analysis tool based on new intrinsic resolution methods. Nuclear Engineering and Design, 2022, 386, pp.111548. 10.1016/j.nucengdes.2021.111548 . hal-03468571

HAL Id: hal-03468571

<https://hal.science/hal-03468571>

Submitted on 5 Jan 2024

HAL is a multi-disciplinary open access archive for the deposit and dissemination of scientific research documents, whether they are published or not. The documents may come from teaching and research institutions in France or abroad, or from public or private research centers.

L'archive ouverte pluridisciplinaire **HAL**, est destinée au dépôt et à la diffusion de documents scientifiques de niveau recherche, publiés ou non, émanant des établissements d'enseignement et de recherche français ou étrangers, des laboratoires publics ou privés.



Distributed under a Creative Commons Attribution - NonCommercial 4.0 International License

RayActive: An all-in-one R2S neutron induced activation analysis tool based on new intrinsic resolution methods.

N. Dray^{a,*}, E. Suraud^b, C. Dossat^a and N. Chatry^a

^aTRAD - Tests & Radiations, 907 Voie L'Occitane, 31670 Labège, France

^bLaboratoire de Physique Théorique - IRSAMC (UMR 5152 CNRS/UPS), Université Paul Sabatier, 118, route de Narbonne bât 3R1B4, 31062 Toulouse Cedex 9, France

ARTICLE INFO

Keywords:

Neutron Induced Activation
Monte-Carlo
R2S
Shutdown Dose Rate
CAD
RayActive

ABSTRACT

Neutron production in nuclear facilities can induce a SDDR (Shutdown Dose Rate) even after months. Different methods exist to simulate the SDDR of neutron activated materials. The most used method is the mesh-based R2S (Rigorous-Two-Steps). This method couples a Monte-Carlo code and an isotopic inventory code to compute the SDDR. The Monte-Carlo code computes the neutron flux on a user-defined mesh to take into account the neutron flux gradients in the cells. The aim of this article is to present RayActive, a prototype tool elaborated for computing the SDDR. RayActive is based on a modified R2S method with an almost exact identification of materials enclosed in each voxel of a superimposed mesh. The CAD based geometry definition for the model makes possible this identification. Moreover, RayActive is designed as an "all-in-one" package without any other code coupling. RayActive is designed to be as easy to use as possible and each part of the computation has been optimized to minimize the computational time. Verification and validation of RayActive has been done on shutdown dose rate benchmarks made with FLUKA code and classical R2S process coupling MCNP and FISPACT codes. Good agreement was found for these benchmarks even if some differences occur for the validation benchmark. These discrepancies show the impact on the results of the modified R2S method employed in RayActive.

1. Introduction

Neutron production in nuclear facilities is at the origin of a phenomenon called neutron induced activation. When neutrons go through surrounding materials they can interact with the nuclei of the atoms that compose these materials. In some cases, these interactions lead to the creation of new nuclei. Sometimes, these nuclei are radioactive and will reach a more stable state by spontaneously disintegrating, i.e. by emitting decay particles such as photons. If a sufficient amount of neutrons have been produced and have interacted with the components of the installation, an ambient dose equivalent rate may be present which can potentially be dangerous for persons approaching neutron activated areas.

To predict the radiological hazards it is convenient to simulate the ambient dose equivalent rate, also called shutdown dose rate (SDDR). Several methods exist for computing the SDDR. The Direct-1-Step (D1S) method [1, 2] computes the SDDR in a single Monte-Carlo transport [3] by replacing the prompt photons by decay photons. A preliminary study is made to compute time correction coefficients. These coefficients are then used to compute the SDDR at the requested time. Another method implemented in FLUKA [4] consists in simulating the decays by a Monte-Carlo process: for every radioactive nucleus produced, a decay time is sampled following the decay time probability. Then, the decay particle is transported to compute the SDDR. Finally, the Rigorous-Two-Step (R2S) method also allows to com-

pute the SDDR. First, a neutron transport is made with a Monte-Carlo code such as MCNP [5]. Then, an inventory code as for example FISPACTII [6] or ACAB [7] computes the inventory at the decay time following the irradiation scenario. The last step is the decay photons transport made with a Monte-Carlo method. The R2S method implementation often couples different nuclear codes.

As the R2S scheme follows the real physical processes, this scheme is used for the new tool. A lot of R2S method validations exist. Some of them are described in [8, 9, 10] and show good agreement of the method with experimental data.

More recently, new features were implemented for the R2S method to overcome some of its limitations. In [11], a fine mesh is used to reach converged neutron flux intensities in voxels and a coarse mesh to get the energy shape of the fluxes. This allows to take into account the neutron flux gradients.

A second issue with the R2S method is the computation of neutron flux in each material enclosed in a voxel. When a cartesian mesh is used, only the average flux in the voxel can be computed which can lead to high discrepancies in results in particular when the voxels enclose a lot of void or air. The MCR2S (Mesh-Coupled R2S) [12, 13] method was designed to overcome this issue. In this methodology, an unstructured mesh composed of tetrahedral voxels is used to adapt the cells of the geometry. The results are in good agreement with other methods even if this method needs more time to give converged Monte-Carlo results.

Another way to make the results more precise than standard R2S is to identify the materials enclosed in each voxel. In [14], a given amount of points is sampled in each voxel

*Corresponding author

ORCID(s): 0000-0002-0856-0630 (N. Dray); 0000-0003-2134-3603 (E. Suraud)

and the material identified for each point is stored. The number of points for which a material is identified in the voxel divided by the number of sampled points gives the volume proportion of the current material in the voxel. This is a Monte-Carlo process, therefore the precision of the results will directly depend on the number of sampled points. This method is also in good agreement with original R2S.

The idea of the modified R2S method presented here is to make the method compatible with an industrial usage. The methodology is therefore designed to overcome some of the R2S limitations while automating and improving the accuracy of the calculation. Moreover, the methodology is conceived to be as generic and reliable as possible. A structured cartesian mesh is thus used for the Monte-Carlo computations to avoid adding complexity to the process. An almost exact identification of cells enclosed in each voxel is done by the use of modern CAD means. The complete computation is made inside only one prototype tool named RayActive and every part of the calculation is designed to be as optimized as possible. The presented methodology of RayActive relies on RayXpert[®] CAD (Computer Aided Design) and Monte-Carlo 3D capacities [15].

The modified R2S method is presented in this paper. In a first part, the description of the new features is done. Then the verification of the features is presented. Next, a validation benchmark is described and its results are shown. Finally, a conclusion is made.

2. Description of the new features

As previously said, the R2S scheme is used to compute the SDDR with RayActive. In the very first part, the model of the geometry is performed.

2.1. Geometry modelling

RayActive relies on the features of RayXpert software. RayXpert is an unique code able to model a geometry by CAD means and to run a Monte-Carlo 3D transport with this model in the same interface. Moreover, RayXpert has a graphical user interface to create the model. So, in RayActive, the model is made with the CAD kernel of RayXpert which is Open Cascade technology [16]. The geometry is therefore in the boundary representation format (B-Rep). RayXpert could also import a STEP model file [17] directly. Monte-Carlo transport is handled by a Ray Tracing algorithm [18]. This allows the spaces between cells to be clearly identified and by defining an ambient material, particles could be transported without needing to construct cells of this material between the components of the geometry. [Figure 1](#) shows a step model and its imported geometry in RayXpert.

2.2. Neutron flux computation

Depending on the modeled geometry, significant neutron flux gradients could exist inside cells. For example, if a punctual neutron source irradiates a block of concrete, the neutron flux will be higher on the side of the cube next to the source than on its opposite side. For this example,

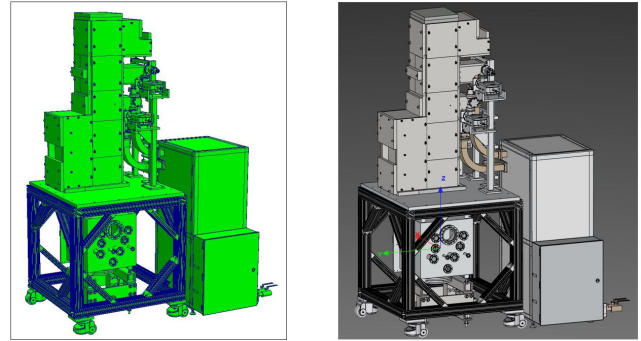


Figure 1: Example of a STEP model (left) and the imported step model in RayXpert (right).

the number of transmuted nuclei should be function of the position inside the cube. Nevertheless, if an average flux is considered in the whole cube, this dependence does not exist. Moreover, in Monte-Carlo code, the neutron flux is computed using the track-length estimator which is defined as :

$$\Phi_{n,detector} = \frac{\sum_{k=1}^q l_k}{NV_{detector}} \quad (1)$$

where

- $V_{detector}$ is the volume of the detector
- l_k is the track length of the k particle through the detector
- q is the amount of particles which went through the detector
- N is the total number of primary particles launched

The flux given by [equation 1](#) is an average flux over a detector. In a Monte-Carlo transport, the detectors are also the geometry cells. Hence, in general, the neutron flux gradients would not be taken into consideration except if the user cuts the cells into smaller cells manually which would be too much time consuming. Therefore, a superimposed mesh is required to take into account the neutron flux gradients. The mesh allows to compute more precisely the isotopic inventory in the geometry as it automatically cuts the cells into voxels.

Multiple type of meshes could be used for this purpose. The mesh could be structured or unstructured; uniform or non uniform; coordinates could be cartesian, cylindrical or spherical. To limit the memory need and the Monte-Carlo computation time, we use here a structured uniform cartesian mesh to compute the neutron flux. Indeed, with a cartesian mesh, the number of voxels is known before running the calculations whereas with a conforming mesh, the number of voxels could be too important and could therefore saturate the available RAM. Moreover, meshing a geometry with a conforming mesh could sometimes fail. So, to respect the

objectives of RayActive (generic method and automation), a cartesian mesh is used for Monte-Carlo neutron flux calculation. The issue with a structured cartesian mesh is the possible mismatch between cells and voxels. The average neutron flux could be directly computed in a voxel but the fluxes for each cell enclosed in the voxel can have big discrepancies between them. So, to improve the accuracy, it is relevant to compute a neutron flux for each cell enclosed in a voxel but this requires the volume proportions of cells in the voxel. In the case where the neutron flux intensity is low enough so that the production rate of an isotope is negligible in comparison with its decay rate, the volume of material is not really needed. Indeed, when computing the isotope production, the volume dependency vanishes because of the neutron flux normalisation of [equation 1](#). However, as RayActive is designed for an industrial usage, it is relevant to use as few assumptions as possible. So, in this context, the volume proportion of each material enclosed in each voxel is needed. It is nevertheless possible to compute a good approximation of the material volumes enclosed in voxels [14] or to conform the mesh to the cells [12]. In the present work a new and unique feature was developed to compute an almost exact volume proportion of each cell enclosed in a voxel. This allows to be even more precise than using a flux for each material enclosed in a voxel as, depending on the voxel size, the neutron flux could significantly differ for cells made of the same material. As the geometric model used for the Monte-Carlo transport and for the geometry construction are the same and are obtained by CAD means, the volume proportions could be computed precisely using CAD features.

For example, the volume of one cube cell of mono-material of 5cm side hollowed out by a centered sphere of 2cm radius was computed with both a 10^3 points Monte-Carlo method and the new method relying on CAD features using one voxel of 5cm side centered on the cell center. The error in the volume proportion with the first method is equal to 6.65% whereas for the second method it is below 0.01%. These results show that the new RayActive functionality performs really well the computation even if the results are not analytical.

As the volume proportion of each cell in a voxel could be accurately computed with RayActive, it is now possible to compute precisely a neutron flux for each cell in a voxel (as the volume of the detector is needed for the neutron flux calculation, see [equation 1](#)). So, with RayActive, the difficulties of the previous methods are overcome; the superimposed uniform cartesian mesh cuts cells into real smaller detectors that could take into account neutron flux gradients.

2.3. Isotopic inventory computation

Once the neutron flux is obtained for each material in a voxel, the inventory for each material after irradiation has to be calculated. The inventory evolution system is a system of coupled ordinary differential equations given in [equation 2](#). To solve this system, the initial inventory has to be known. Another advantage of the accurate computation of volume proportions of cells enclosed in voxels is that the initial in-

ventory of each material inside the voxel is also accurately computed. Moreover, it also allows to find any small cells that could be enclosed in a voxel and could contribute noticeably to the SDDR. The new method thus allows both the neutron flux and the initial inventory of material to be more accurate.

$$\begin{aligned} \frac{dN_i(t)}{dt} &= -N_i \cdot [\lambda_i + \xi_i] + \sum_{\substack{j=1 \\ j \neq i}}^r N_j \cdot [\lambda_{j \rightarrow i} + \xi_{j \rightarrow i}] \\ \xi_i &= \int_0^{+\infty} \sigma_i(E) \Phi(E) dE \\ \xi_{j \rightarrow i} &= \sum_{q=1}^M \int_0^{+\infty} \sigma_{q,j \rightarrow i}(E) \Phi(E) dE \end{aligned} \quad (2)$$

where :

- $N_i(t)$ is the number of nuclei of isotope i at time t with initial value $N_{i,0}$
- r is the total number of isotopes available in the database
- M is the number of transmutation reactions
- $\sigma_i(E)$ is the total cross section for isotope i at energy E (in barn)
- $\sigma_{q,j \rightarrow i}(E)$ is the transmutation cross section from isotope j to isotope i for reaction q at energy E (in barn)
- Φ is the neutron flux computed from the Monte-Carlo transport for the considered cell (cm^{-2}/s)
- λ_i is the decay constant of isotope i to any of its decay isotopes (in s^{-1})
- ξ_i is the total transmutation rate of isotope i under neutron flux Φ with isotope i total neutron cross section σ_i (in s^{-1})
- $\lambda_{j \rightarrow i}$ is the decay constant of isotope j to isotope i (in s^{-1})
- $\xi_{j \rightarrow i}$ is the average production rate of isotope i under neutron flux Φ from isotope j (in s^{-1})

To compute the inventory after irradiation, the system defined by [equation 2](#) has to be solved. The issue with this problem is that the equations are "stiff". A problem is said stiff when the ratio of coefficients that link unknowns between them is very high which is the case here because some decay constants are very high (up to 10^8s^{-1}) and other ones very low (down to 10^{-12}s^{-1}). When a system of ODE is stiff, the use of a BDF (Backward Differentiation Formula) [19]

is mandatory. In such a case, other methods such as Runge-Kutta or Adams-Bashforth will never give correct results in a reasonable time. BDF is a predictor/corrector method that computes an approximate solution of the system at the next step. Then this solution is corrected by solving a linear system that couples both the approximate solution and its derivative.

New methods were recently developed to reach an even better accuracy. These methods are called BBDF (Block BDF) and consists in solving the system for the two next steps at the same time. Some of these methods are presented in [20, 21, 22, 23]. Based on the method presented in [20], an internal stiff ODE solver was developed and integrated to RayActive to solve as efficiently as possible the inventory system.

A verification and validation of the solver have been made and show good agreement between RayActive ODE solver and LSODE [24] (a well known and validated ODE solver) for the Gear's problem [19]. An inventory problem where a cube (side = 1cm) of pure ^{56}Fe (density = 1.0g/cm³) is irradiated during 10 years by a punctual, mono-kinetic energy (14MeV), isotropic, centered in the cube, continuous source of intensity equal to 10¹⁶ neutron/s has also been made. The solutions with both RayActive and FISPACTII code [6] (whose ODE solver is LSODE) have been compared. Coherent results were found between the two methods even if discrepancies appeared for some isotopes. The origin of these discrepancies have been identified and will be published in a future article. Changes have been made to adapt the new method to FISPACTII and the inventory benchmark presented here has been made again. For this benchmark, the initial number of nuclei of ^{56}Fe is 1.075382×10^{22} and the total neutron flux computed in the cube by the Monte-Carlo process is equal to 6.13762×10^{15} neutrons/cm²/s. A large enough number of source particles were emitted to ensure that the neutron flux uncertainties are below 10% for every group that contributes at least 0.1% to the total flux. The relative tolerance used was 10⁻⁴ and the absolute tolerance was 10³ for both inventory code. The meaning of these tolerances is given in [24]. The inventory is requested after 10 years. Table 1 shows the inventory for FISPACTII and RayActive. Table 1 also shows the relative difference R_{rel} defined by equation 3 where FISPACTII results are used as reference. For readability reason, the results were filtered in table 1 by only showing the results with isotope nuclei amount over $10^{-4} \times N_{56\text{Fe}}(t = 0)$.

$$R_{\text{rel}} = \frac{N_i(t)_{\text{computed}}}{N_i(t)_{\text{reference}}} - 1 \quad (3)$$

From results presented in table 1, a very good agreement could be seen between FISPACTII results and RayActive prototype method results. Indeed, for all the presented isotopes in table 1 the relative difference is below 0.6% and for some isotopes, the amount is the same (as for example for ^{54}Cr) taking into account the numerical precision. Moreover, for the whole inventory (containing 161 isotopes

Isotope	FISPACTII	RayActive	Rel. difference
^1H	3.93E+21	3.93E+21	2.54E-04%
^2H	9.12E+19	9.12E+19	3.29E-04%
^4He	9.86E+20	9.86E+20	1.01E-04%
^{47}Ti	2.36E+18	2.37E+18	2.96E-01%
^{48}Ti	1.40E+19	1.41E+19	5.30E-01%
^{49}Ti	2.98E+19	2.98E+19	1.91E-01%
^{50}Ti	2.37E+19	2.37E+19	8.45E-04%
^{49}V	4.48E+18	4.48E+18	1.32E-02%
^{50}V	4.48E+19	4.48E+19	1.56E-03%
^{51}V	1.61E+20	1.61E+20	1.25E-03%
^{51}Cr	4.34E+18	4.34E+18	2.30E-03%
^{52}Cr	7.99E+20	7.99E+20	2.50E-04%
^{53}Cr	6.43E+20	6.43E+20	3.11E-04%
^{54}Cr	1.04E+21	1.04E+21	0.00E+00%
^{53}Mn	3.07E+20	3.07E+20	3.25E-04%
^{54}Mn	3.19E+20	3.19E+20	0.00E+00%
^{55}Mn	2.05E+21	2.05E+21	0.00E+00%
^{54}Fe	3.37E+20	3.37E+20	0.00E+00%
^{55}Fe	9.31E+20	9.31E+20	5.37E-04%
^{56}Fe	4.03E+21	4.03E+21	2.48E-04%
^{57}Fe	3.46E+18	3.46E+18	2.89E-04%

Table 1

Inventory for FISPACTII and RayActive for the presented benchmark, at $t = 10$ years and value of the relative difference associated.

for both codes), the maximum relative difference is -0.714% for ^{12}C , which also shows a really good agreement. Note that ^{12}C is not included in table 1 as its amount is very small.

2.4. SDDR map calculation

Since the inventory at decay time is computed for each cell in each voxel, it is now possible to compute the SDDR map. To proceed, the decay particles have to be transported with Monte-Carlo. As the most dangerous particles (in terms of radiological hazard) are the photons, only this type of particles is followed in the second Monte-Carlo to speed up the SDDR computation.

In reality, a lot of decay photons could be emitted as a huge amount of radioactive isotopes could have been produced in each voxel of the mesh. To compute the SDDR in a reasonable duration, cumulative PDF (probability density functions) are computed in RayActive to sample the decay particles. In the new prototype tool, two sampling schemes are available. In the first one, the intensity of a decay photon ray divided by the whole model's intensity is used as the emission probability. In the second one, the product energy times intensity of a decay photon ray divided by the whole model energy times intensity values is used as the emission methods. Appendix A presents the details of this sampling process. The second sampling process is based on the hypothesis that the photons with higher energy contributes more to the SDDR than the lower energy photons. With the second sampling method, higher energy decay photons will thus be more sampled than lower energy ones which should speed up the total SDDR convergence during the Monte-

Carlo process. A correction of the photon weights is made to adjust the probability biasing.

To compute the parameters of the decay photons, depending on the sampling method requested, a random number between 0 and 1 is sampled. Then the ray corresponding to the random number simulated is identified using one of the two sampling probability described previously and detailed in [appendix A](#). The ray identification using PDF also allows to find the mesh, voxel, material and cell from where the decay photons will be emitted and their energy as the cumulative PDF is constructed over these quantities.

To get the emission position of the decay photon, a random position in the voxel is sampled. If the material identified at the sampled position corresponds to the material sampled with the cumulative PDF, then this position is accepted. Otherwise, another position is sampled either until the correct material and cell are found or until a limit of attempts defined by the user is reached. If the limit is reached, the process returns to the beginning of the sampling.

To avoid irrelevant position sampling that would cost a lot of computation time, the user could also specify another parameter. First, the product of a cell volume with its energy-intensity value is defined by [equation 4](#).

$$P_i = V_i \sum_{j=1}^{m_i} \sum_{k=1}^{p_j} E_{i,j,k} I_{i,j,k} \quad (4)$$

where :

- V_i is the volume of cell i in voxel
- m_i is the number of radioactive isotopes in cell i
- p_j is the number of photon decay ray for isotope j in cell i
- $E_{i,j,k}$ is the energy of ray k for isotope j in cell i
- $I_{i,j,k}$ is the intensity of ray k for isotope j in cell i

Then the total product of cell volume with its energy-intensity of a voxel is defined by [equation 5](#). The user can thus specify the value of the ratio $\frac{P_i}{P_{tot}}$ over which the cell i is allowed to emit decay particles. Indeed, the higher its intensity and energy, the higher the decay ray contributes to SDDR. By using this parameters, only the low volume and low contribution to SDDR photon decay sources will be skipped instead of all small volume photon decay sources (if filtered by volume proportion).

$$P_{tot} = \sum_{i=1}^n P_i \quad (5)$$

where :

- n is the number of cells in the voxel
- P_i is the product of a cell i volume with its energy-intensity defined by [equation 4](#)

Finally, the photon flux computed by Monte-Carlo 3D method is converted to SDDR by flux-to-dose conversion factors given in [25]. A verification of the presented activation prototype method is made in the next section.

3. Verification of RayActive results

To verify RayActive neutron induced activation analysis capacities, two simple benchmarks were realised with RayActive and by two other means. The first process used to compute the SDDR of the simple benchmarks was a classical R2S technique coupling MCNP6.2 [26] and FISPACT codes. The second code used is FLUKA which is able to compute neutron induced activation and SDDR map in the same run. The activation method used in FLUKA can process the activation by two different methods. The first method is a Monte-Carlo process that computes randomly the decay time of any radioactive nucleus produced during neutron transport. The second method computes the production rates of each isotope then solves analytically the inventory at the requested time instead of randomly sampling the decay time. As the second method better matches to the R2S method, this method is used for the verification benchmark first presented in [27].

3.1. Geometry and parameters

The geometry of the verification benchmarks presented in [figure 2](#) is composed of three cubes, each of the same side equal to 1cm. The center of a cube is at its origin and cartesian coordinates are used for both benchmarks (x,y,z) with cm as length unit. The source cube is centered at the point O(0,0,0) for the two benchmarks and its material is air of density $d_{Air}=0.001205\text{g/cm}^3$. The two other cubes are centered at points $P_1(-20.5\text{cm},0,0)$ and $P_2(20.5\text{cm},0,0)$ respectively. For first benchmark (noted #1), the two cubes are both composed of the same material which is pure ^{59}Co ($d_{Co}=8.9\text{g/cm}^3$). For the second benchmark (#2), the cubes are made of stainless steel (SS316LN, $d_{SS316LN}=7.8\text{g/cm}^3$). The material compositions are described in [appendix B](#). The neutron source is, for the two benchmarks, the cell centered at point O. It is isotropic, mono-kinetic (14MeV) and its intensity is 10^{12}n/s . The irradiation scenario is 30.5 days of irradiation at intensity of 10^{12}n/s followed by two hours cooling (zero intensity). The SDDR map is computed at the end of the 2h cooling on a cartesian mesh centered on O, with dimensions $100\text{cm}*100\text{cm}*100\text{cm}$ and 100 voxels per direction. The environment material is for both benchmarks air.

3.2. Results and analysis

The SDDR map was computed with MCNP6.2 and FISPACT combination, FLUKA and RayActive. [Figure 3](#) shows the final SDDR map at $y=0.0\text{cm}$ for benchmark #1 (Co) obtained with FLUKA, [figure 4](#) shows the one obtained with RayActive and [figure 5](#) the one obtained with MCNP and FISPACT combination. There is a good agreement between the three methods even if for FLUKA some lines can be seen. These lines may correspond to a lack of convergence due to

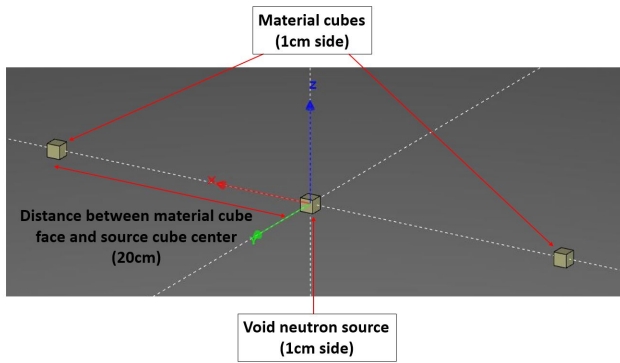


Figure 2: Geometry used for verification benchmarks.

the simulation performance of induced activation of FLUKA code (as the amount of simulated particles is equivalent for each of the three methods used). The SDDR maps for benchmarks #2 (SS316LN) are in appendix C and also shows a good agreement between results of all processes.

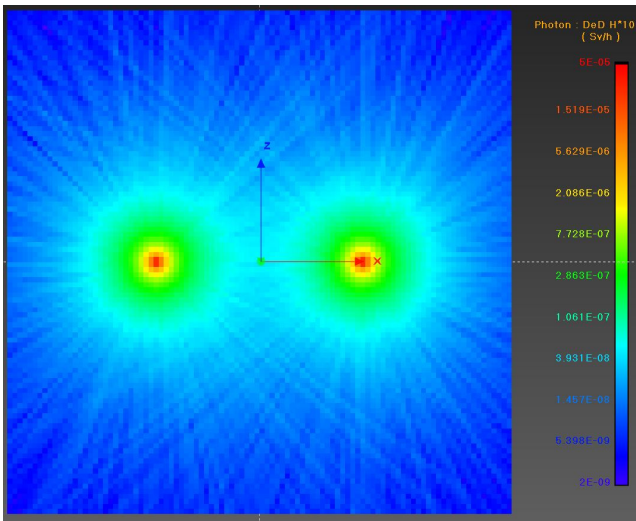


Figure 3: SDDR map at $y=0.0\text{cm}$ for benchmark #1 (Co) obtained with FLUKA.

To compare the results more precisely, the SDDR value was computed along x axis at $y=0\text{cm}$ and $z=0\text{cm}$. The results for benchmark #1 (Co) is shown in figure 6 and for benchmark #2 (SS316LN) in figure 7. For benchmark #1 (Co) a good agreement is observed between FLUKA, RayActive and MCNP/FISPACT combination with all relative differences (MCNP/FISPACT as reference) below 5%. For benchmark #2 (SS316LN), the curve shapes look similar but the results seems to be slightly higher for RayActive than the results for MCNP/FISPACT and FLUKA.

The relative difference (MCNP/FISPACT as reference) along x axis at $y=0.0\text{cm}$ and $z=0.0\text{cm}$ for benchmark #2 (SS316LN) is presented in figure 8. From figure 8, it can be seen that the results from RayActive are higher than the results from MCNP/FISPACT; on average, the results are 7.63% higher. On the contrary, results for FLUKA are on

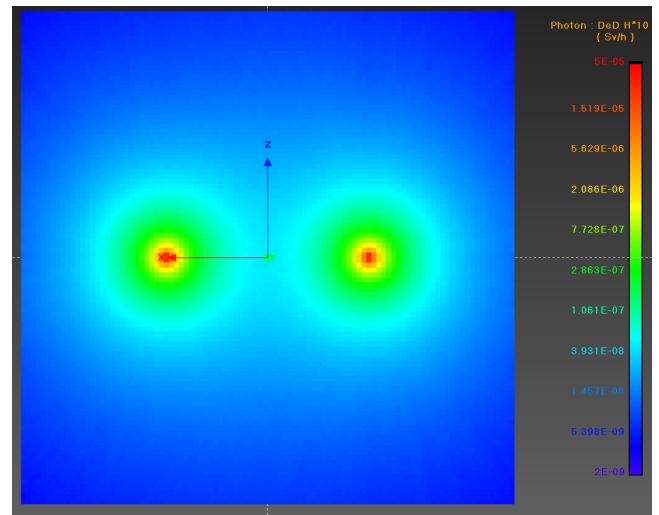


Figure 4: SDDR map at $y=0.0\text{cm}$ for benchmark #1 (Co) obtained with RayActive.

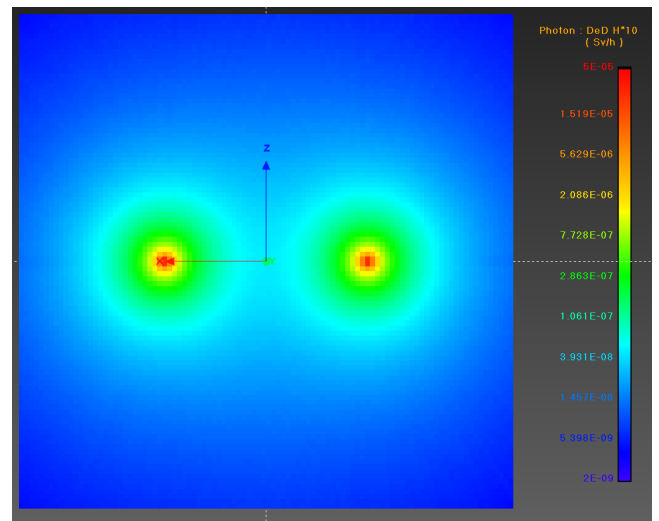


Figure 5: SDDR map at $y=0.0\text{cm}$ for benchmark #1 (Co) obtained with MCNP and FISPACT combination.

average 5.74% lower than the results from MCNP/FISPACT. These discrepancies could have different origins. First of all, FLUKA uses other cross sections than MCNP/FISPACT and RayActive. Indeed, the FLUKA cross sections used for the benchmarks are from ENDF/BVI.8, ENDF/BVII.0 and JENDL3-3 [28, 29, 30] whereas ENDF/BVII.1 [31] is used for neutron transport and TENDL2017 [32] for inventory computation in both MCNP/FISPACT and RayActive. Moreover, FLUKA cross sections are averaged on 260 energy groups whereas MCNP/FISPACT and RayActive transport cross sections are point-wise. Finally, RayActive generates point-wise energy decay particles whereas MCNP/FISPACT generates decay particles energy from averaged energy groups. However, in neutron induced activation analysis, referring to [10, 13, 27], discrepancies below 10% are considered as being in good agreement.

So, even if the SDDR results for benchmark #2 (SS316LN)

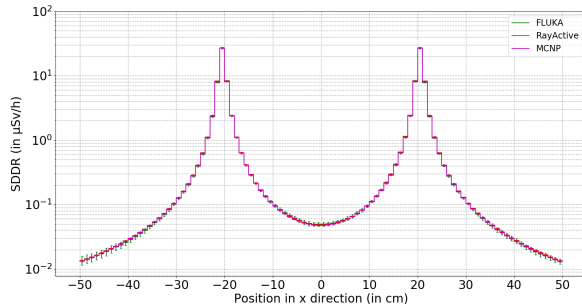


Figure 6: SDDR along x axis at $y=0.0\text{cm}$ and $z=0.0\text{cm}$ for benchmark #1 (Co) with propagated Monte-Carlo uncertainties.

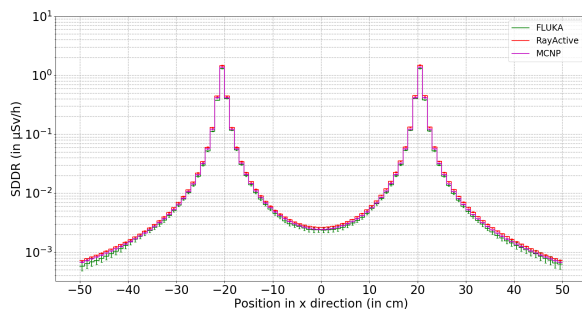


Figure 7: SDDR along x axis at $y=0.0\text{cm}$ and $z=0.0\text{cm}$ for benchmark #2 (SS316LN) with propagated Monte-Carlo uncertainties.

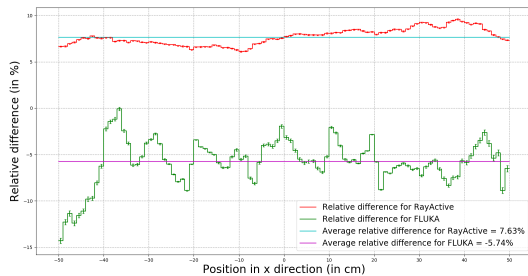


Figure 8: Relative difference between RayActive and MCNP/FISPACT and between FLUKA and MCNP/FISPACT (MCNP/FISPACT as reference) at $y=0.0\text{cm}$ and $z=0.0\text{cm}$ along x axis for benchmark #2 (SS316LN) with propagated Monte-Carlo uncertainties.

are slightly higher with RayActive and lower for FLUKA in comparison with reference R2S, it seems that RayActive performs well the SDDR computation in these cases. In fact, for benchmark #2 (SS316LN), the discrepancies could have different origins. Moreover, with the simpler benchmark #1 (Co) with only one isotope, the results are in good agreement between the three methods. Another benchmark has been done to ensure that the SDDR computed with RayActive performs well. This benchmark is presented in the next section.

4. Validation benchmark

The previous benchmarks seem to show good agreement between classical R2S and RayActive neutron induced activation results. To ensure that RayActive is able to compute the SDDR in a more general way, another more complex benchmark was made. This benchmark is based on a model of an experimental setup used to measure neutron scattering cross section. The geometry of the model is presented on figure 9.

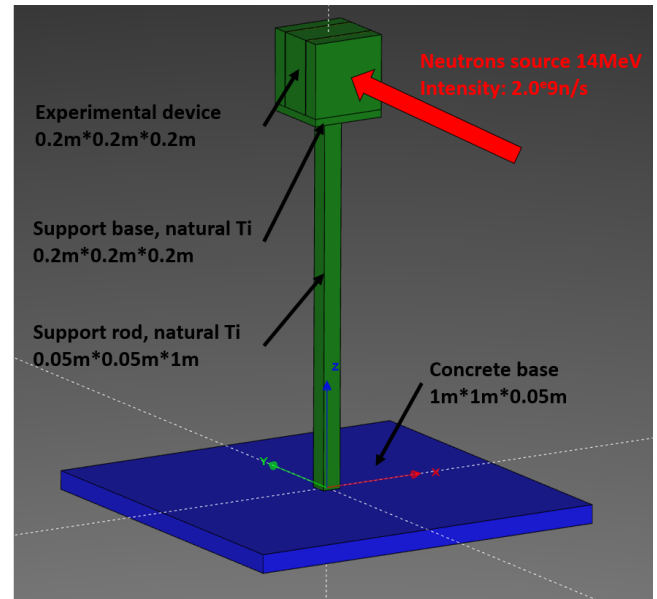


Figure 9: Model of the experimental setup used for validation benchmark.

An experimental device is irradiated by a fixed parallel to $+y$ direction neutron source. The source is a disc of radius $R=5\text{cm}$ with origin at $S(0.0, -40.0\text{cm}, 112.0\text{cm})$. The source intensity is set at $2.0 \times 10^9 \text{ n/s}$ for 30 days followed by one day of cooling. The base is a bloc of $1\text{m} \times 1\text{m} \times 0.05\text{m}$ dimensions. It is made of concrete ($d_{\text{Concrete}}=2.3\text{g/cm}^3$) and its center is at the position $C(0.0, 0.0, -2.5\text{cm})$. The support rod and base are placed on the concrete bloc. They are both made of natural Ti ($d_{\text{Ti}}=4.5\text{g/cm}^3$). The experimental device is a bloc of 20cm side. It is composed of 3 layers of natural Ti (two of 4.8cm length and the center one of 10cm length). Two layers of natural gold ($d_{\text{Au}}=19.3\text{g/cm}^3$) of 0.2cm length are placed between the Ti layers. All the dimensions and placement are presented on figures 9 and 10. The environment material is air of density $d_{\text{Air}}=0.001205\text{g/cm}^3$. Finally, all the compositions of the materials used for this benchmark are given in appendix D.

The SDDR was calculated both with RayActive and with the coupling of MCNP/FISPACT. The SDDR map for $x>0$ obtained with RayActive is plotted on figure 11 and the one computed with MCNP/FISPACT is presented on figure 12. Both calculations deliver comparable results, qualitatively very similar, albeit with slight quantitative differences. Indeed, the area where the SDDR is greater than 100.0mSv/h is larger on the MCNP/FISPACT map than on the one from

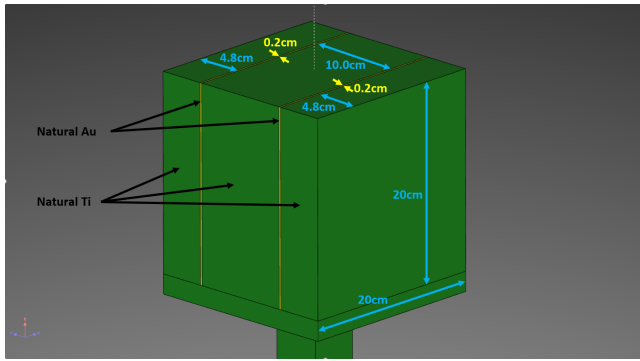


Figure 10: Enlarged view of the experimental device used for the validation benchmark.

RayActive. The other areas have the same behavior. They are larger for MCNP/FISPACT. Nevertheless, the shapes of the zones seem to be in good agreement between both computations with larger SDDR on the side of the neutron source ($y < 0$). To extent the comparison between both approaches, the SDDR along the y axis at the center of the experimental device ($x=0\text{cm}, z=112\text{cm}$) has been plotted both for RayActive and MCNP/FISPACT on figure 13.

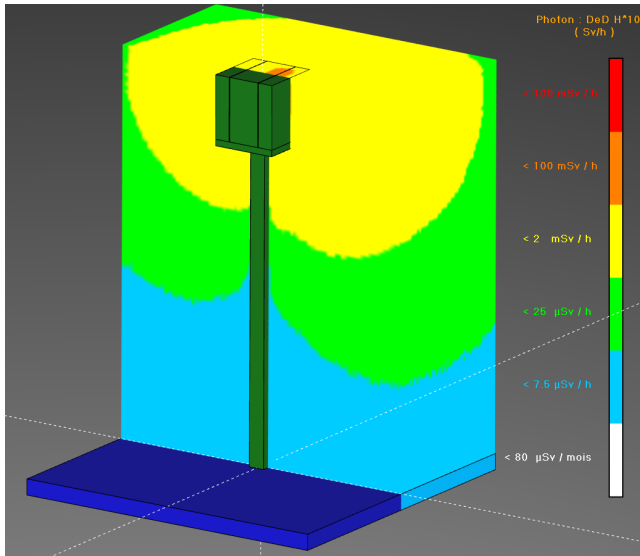


Figure 11: Mapping of SDDR for $x > 0$ for the model of the experimental setup obtained with RayActive.

From figure 13, it can be seen that the SDDR for MCNP/FISPACT is larger than the SDDR obtained with RayActive all along the y axis. Nevertheless, the shapes of the curves are in rather good agreement down to tiny details such as the asymmetry between positive and negative y positions. The SDDR is higher for the negative y than for the positive y . This asymmetry could come from the neutron source which emits neutrons from the negative values of y in the positive y direction. Moreover, two small peaks could be seen at the positions of the gold layers (at $x = \pm 5.1\text{cm}$) both for RayActive and MCNP/FISPACT. Discrepancies between RayActive and MCNP/FISPACT could be attributed to the

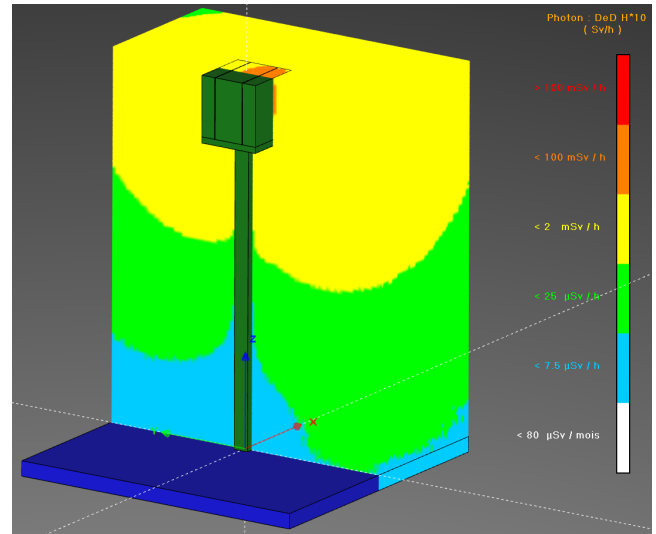


Figure 12: Mapping of SDDR for $x > 0$ for the model of the experimental setup obtained with MCNP/FISPACTII.

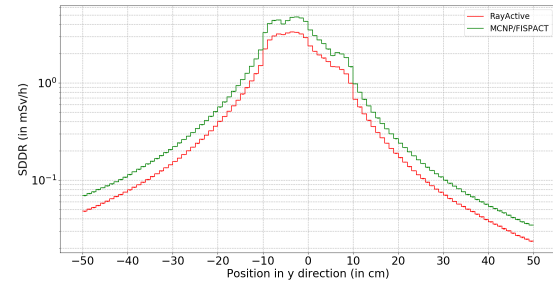


Figure 13: SDDR along the y axis at $x=0.0\text{cm}$ and $z=112.0\text{cm}$ for RayActive and MCNP/FISPACT for the experimental device benchmark.

the neutron flux computation with MCNP. Indeed, MCNP distribution we have access to does not allow to compute a neutron flux for each cell enclosed in a voxel. The neutron flux is thus computed for a whole voxel as it is done in the classical R2S scheme. As a voxel can superimpose different materials, the neutron flux can be overestimated. Indeed, in air the neutron flux is generally higher than in a solid material because the density of air is significantly lower. The mean free path of particles in gas is thus greater than in dense material. However, a larger mean free path of particles implies a larger flux as can be seen from equation 1. Therefore, when a voxel superimposes air and materials, the average neutron flux computed for the voxel and used for the isotopic inventory computations will be higher than the real neutron fluxes in each of the enclosed materials. In RayActive, the real neutron flux in the material is specifically computed which is not the case with MCNP/FISPACT.

Moreover, two peaks are visible at the positions of the centers of the gold layers and discrepancies between MCNP/FISPACT and RayActive are reduced in these areas. From figure 13, it is possible to see that these positions correspond to SDDR local maxima. Once again, the same mech-

anism of superimposition might explain this effect. Indeed, in MCNP/FISPACT the voxels that superimpose the experimental device could contain natural Ti and natural Au. As gold has a higher density than titanium ($d_{\text{Au}} = 19.3\text{g/cm}^3 > d_{\text{Ti}} = 4.5\text{g/cm}^3$), the average neutron flux computed for voxels that superimpose both Au and Ti will be lower than the neutron flux computed only for Au which will again affect the inventory for gold layers in MCNP/FISPACT. Therefore, the neutron fluxes used for gold layers isotopic inventory computations with MCNP/FISPACT are likely to be lower than the ones used with RayActive in which the neutron flux is computed for Au only. These differences between the SDDR results are interesting as they suggest a significant dependence on the way the neutron flux is computed, especially when different materials are involved. A complete analysis of such effects goes beyond the scope of this work and will be considered in a forthcoming publication.

5. Conclusion

In conclusion, RayActive is a new tool designed to perform neutron induced activation analysis. The geometry modelling is based on CAD. The algorithm used is a R2S scheme which is an accurate process as it respects the physical steps. The neutron flux is computed on a structured cartesian uniform mesh which reduces the complexity of the method and increases the performance of the Monte-Carlo step. Moreover, RayActive has the unique ability to compute an almost exact cell volume proportion enclosed in a voxel. This allows both to improve the neutron flux computation and the initial isotope inventory in comparison to a classical R2S computation. Furthermore, the inventory system is solved using a new variable step size BBDF solver which is more stable and precise than BDF solver. Then, the decay particles transport convergence could be accelerated with a new decay source sampling method adapted to the SDDR evaluation context. Finally, all these steps are unified in the same prototype method which makes the solution more stable and avoid code interface. Verification on benchmarks have been made and seem to give coherent results even if small discrepancies have been seen. Validation benchmark has been made on a more complex geometry. It also shows coherent results even if some discrepancies are noticeable in comparison with the traditional R2S computation. The difference could come from the neutron flux computation which is averaged on the whole voxel with the classical R2S. As the neutron flux is computed for each cell enclosed in voxel in RayActive, its results should be more precise. Nevertheless, these discrepancies will be investigated in more details in a further work to ensure that it comes from the neutron flux computation.

Acknowledgements

This work was supported by the Laboratoire de Physique Théorique de Toulouse, Toulouse, France; and TRAD - Tests & Radiations, Labège France

A. Decay ray sampling methods available in RayActive

The unbiased probability $p_{\text{unbiased},i}$ of emission of a decay ray i is defined by [equation 6](#).

$$p_{\text{unbiased},i} = \frac{I_i}{N} \quad (6)$$

where

- I_i is the decay ray i intensity
- N is the total number of decay rays in the considered material

The biased probability $p_{\text{biased},i}$ of emission of a decay ray i is defined by [equation 7](#).

$$p_{\text{biased},i} = \frac{I_i \cdot E_i}{N} \quad (7)$$

where

- I_i is the decay ray i intensity
- E_i is the decay ray i energy
- N is the total number of decay rays in the considered material

In RayActive, both biased and unbiased decay ray sampling methods are available. A random number l is sampled between 0 and 1. If unbiased sampling method is requested, then decay i is chosen if $p_{\text{unbiased},i-1} \leq l < p_{\text{unbiased},i}$. If biased sampling method is requested, then decay i is chosen if $p_{\text{biased},i-1} \leq l < p_{\text{biased},i}$. In the case where biased probability is used, then the statistical weight w_i of the simulated particle in the Monte-Carlo (which corresponds to the number of particles that the simulated particle represents) is equal to

$$w_i = \frac{\sum_{i=0}^N I_i \cdot E_i}{E_i \cdot \sum_{i=0}^N I_i} \quad \text{in order to have } p_{\text{biased},i} * w_i = p_{\text{unbiased},i}$$

If unbiased probability is used, then $w_i = 1$. Thus, for the Monte-Carlo transport, the flux is computed by taking into account the particle weight which is done by transforming [equation 1](#) into [equation 8](#).

$$\Phi_{n,detector} = \frac{\sum_{k=1}^n w_k \cdot I_k}{NV_{detector}} \quad (8)$$

with w_k the weight of a particle.

B. Material compositions for verification benchmarks

Isotope	Mass fraction (in %)
^{12}C	0.0124%
^{14}N	75.5268%
^{16}O	23.1781%
^{40}Ar	1.2827%

Table 2

Air composition used for verification benchmarks.

Isotope	Mass fraction (in %)
^{59}Co	100.0000%

Table 3

Cobalt composition used for verification benchmark #1.

Isotope	Mass fraction (in %)
^{12}C	0.0065%
^{13}C	0.0001%
^{28}Si	0.4680%
^{29}Si	0.0246%
^{30}Si	0.0168%
^{31}P	0.0253%
^{32}S	0.0165%
^{33}S	0.0001%
^{34}S	0.0008%
^{50}Cr	0.7282%
^{52}Cr	14.604%
^{53}Cr	1.6879%
^{54}Cr	0.4281%
^{55}Mn	1.9930%
^{54}Fe	3.8373%
^{56}Fe	62.465%
^{57}Fe	1.4684%
^{58}Fe	0.1988%
^{58}Ni	8.0841%
^{60}Ni	3.2212%
^{61}Ni	0.1424%
^{62}Ni	0.4614%
^{64}Ni	0.1213%

Table 4

SS316LN composition used for verification benchmark #2.

C. SDDR maps for verification benchmark #2 (SS316LN)

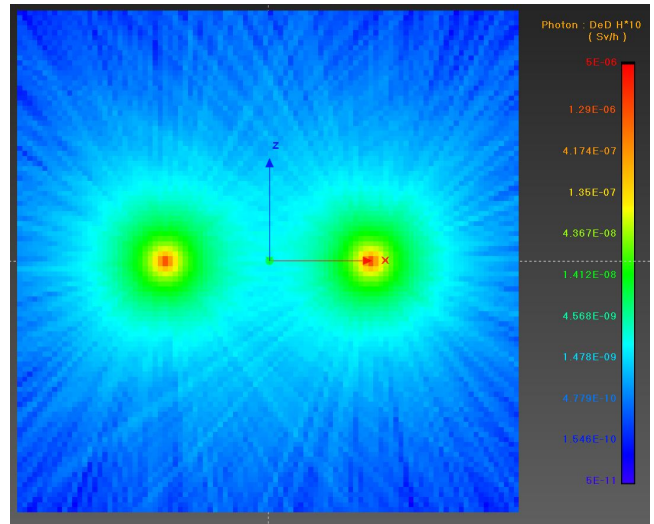


Figure 14: SDDR map at $y=0.0\text{cm}$ for benchmark #2 (SS316LN) obtained with FLUKA.

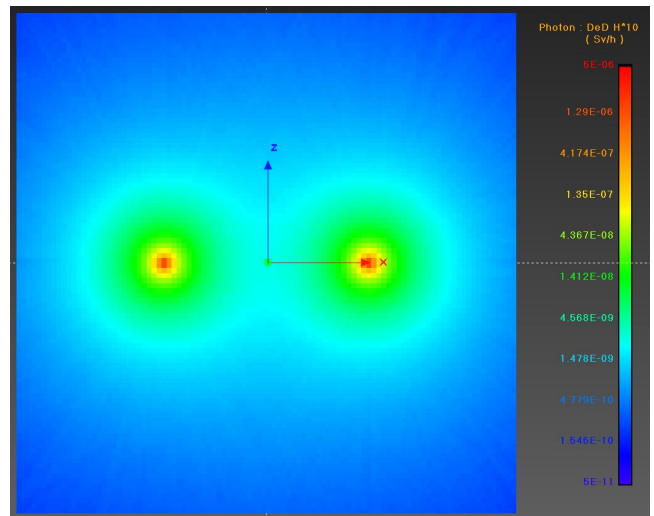


Figure 15: SDDR map at $y=0.0\text{cm}$ for benchmark #2 (SS316LN) obtained with RayActive.

D. Material used for validation benchmark

Isotope	Mass fraction (in %)
^{12}C	0.0124%
^{14}N	75.5268%
^{16}O	23.1781%
^{40}Ar	1.2827%

Table 5

Air composition used for validation benchmark.

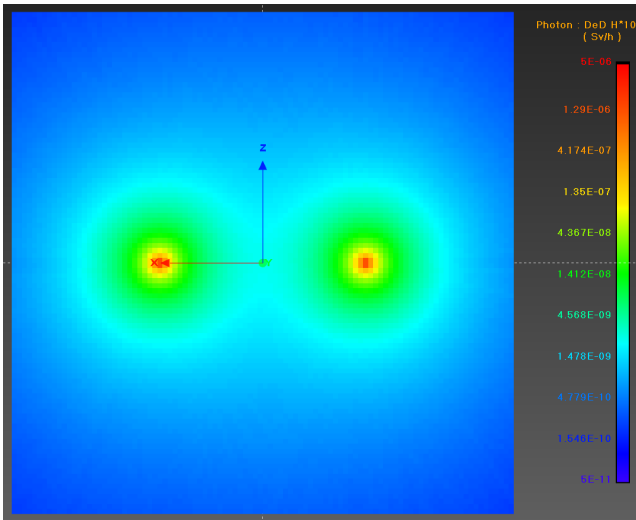


Figure 16: SDDR map at $y=0.0\text{cm}$ for benchmark #2 (SS316LN) obtained with MCNP and FISPACT combination.

Isotope	Mass fraction (in %)
^{197}Au	100.0000%

Table 6

Gold composition used for validation benchmark.

Isotope	Mass fraction (in %)
^{46}Tl	7.9201%
^{47}Tl	7.2978%
^{48}Tl	73.8451%
^{49}Tl	5.5322%
^{50}Tl	5.4049%

Table 7

Titanium composition used for validation benchmark.

Isotope	Mass fraction (in %)
^1H	2.2100%
^{12}C	0.2484%
^{16}O	57.4930%
^{23}Na	1.5208%
^{24}Mg	0.1226%
^{27}Al	1.9953%
^{28}Si	30.4627%
^{39}K	1.0045%
^{40}Ca	4.2951%
^{56}Fe	0.6435%

Table 8

Concrete composition used for validation benchmark.

References

- [1] D. Valenza, H. Iida, R. Plenteda, R. T. Santoro, Proposal of shutdown dose estimation method by Monte Carlo code, *Fusion Engineering and Design* 4 (55) (2001) 411–418.
- [2] R. Villari, U. Fischer, F. Moro, P. Pereslavtsev, L. Petrizzi, S. Podda, A. Serikov, Shutdown dose rate assessment with the Advanced D1S method: Development, applications and validation, *Fusion Engineering and Design* 89 (9-10) (2014) 2083–2087. doi:10.1016/j.fusengdes.2014.01.071.
- [3] R. Y. Rubinstein, D. P. Kroese, *Simulation and the Monte Carlo Method*, Wiley Series in Probability and Statistics, John Wiley & Sons, Inc., Hoboken, NJ, USA, 2016. doi:10.1002/9781118631980.
- [4] A. Ferrari, P. R. Sala, A. Fasso, J. Ranft, FLUKA : A multi-particle transport code, Manuel D’Utilisateur CERN–2005–010 INFN TC 05/11 SLAC–R–773, CERN, Genève (2011).
- [5] X. M. C. Team, MCNP-A General Monte Carlo N-Particle Transport Code: Version5 User’s Guide, Tech. Rep. LA-CP-03-0245, Los Alamos National Laboratory (2005).
- [6] J. C. Sublet, J. W. Eastwood, J. G. Morgan, M. R. Gilbert, M. Fleming, W. Arter, FISPACT-II: An Advanced Simulation System for Activation, Transmutation and Material Modelling, *Nuclear Data Sheets* 139 (2017) 77–137. doi:10.1016/j.nds.2017.01.002.
- [7] J. Sanz, O. Cabellos, N. García-Herranz, ACAB 2008: Activation Code V2008, Tech. Rep. NEA-1839, NEA Data Bank, Issy-les-Moulineaux, France (2008).
- [8] L. Petrizzi, P. Batistoni, H. Iida, D. Valenza, Improvement and benchmarking of the new shutdown dose estimation method by Monte Carlo code, *Advanced Monte Carlo for radiation physics, particle transport simulation and applications. Proceedings* (2001).
- [9] Y. Chen, U. Fischer, Rigorous MCNP based shutdown dose rate calculations: Computational scheme, verification calculations and application to ITER, *Fusion Engineering and Design* 63–64 (3) (2002) 107–114.
- [10] L. Petrizzi, P. Batistoni, S. Migliori, Y. Chen, U. Fischer, P. Pereslavtsev, M. Loughlin, A. Secco, Two computational approaches for Monte Carlo based shutdown dose rate calculation with applications to the JET fusion machine, in: *International Conference on Supercomputing in Nuclear Applications SNA’2003*, Paris, France, 2003.
- [11] M. Majerle, D. Leichtle, U. Fischer, A. Serikov, Verification and validation of the R2Smesh approach for the calculation of high resolution shutdown dose rate distributions, *Fusion Engineering and Design* 87 (5-6) (2012) 443–447. doi:10.1016/j.fusengdes.2011.12.010.
- [12] T. Eade, D. Stonell, A. Turner, MCR2S unstructured mesh capabilities for use in shutdown dose rate analysis, *Fusion Engineering and Design* 100 (2015) 321–333. doi:10.1016/j.fusengdes.2015.06.189.
- [13] A. Turner, Z. Ghani, J. Shimwell, Comparison of Shutdown Dose Rate Results using MCNP6 Activation Capability and MCR2S, Tech. Rep. ARP-097, CCFE (Jul. 2014).
- [14] P. Sauvan, J. P. Catalán, F. Ogando, R. Juárez, J. Sanz, Development of the R2SUNED Code System for Shutdown Dose Rate Calculations, *IEEE Transactions on Nuclear Science* 63 (1) (2016) 375–384. doi:10.1109/TNS.2015.2507138.
- [15] J. C. Thomas, RayXpert Manuel d’utilisation, Tech. Rep. TRAD/DL/DOS/RAYXPRT/CD/110412, TRAD - Tests & Radiations (Nov. 2018).
- [16] O. Cascade, Open CASCADE Technology - Open Cascade.
- [17] S. J. Kemmerer, S. J. Kemmerer, STEP, the grand experience, Tech. Rep. NIST SP 939, National Institute of Standards and Technology, Gaithersburg, MD (1999). doi:10.6028/NIST.SP.939.
- [18] A. Schmitt, H. Müller, W. Leister, Ray Tracing Algorithms — Theory and Practice, in: R. A. Earnshaw (Ed.), *Theoretical Foundations of Computer Graphics and CAD*, Springer Berlin Heidelberg, Berlin, Heidelberg, 1988, pp. 997–1030.
- [19] C. W. Gear, The automatic integration of ordinary differential equations, *Communications of the ACM* 14 (3) (1971) 176–179. doi:10.1145/362566.362571.
- [20] H. Musa, M. B. Suleiman, F. Ismail, N. Senu, Z. B. Ibrahim, An Accurate Block Solver for Stiff Initial Value Problems, *ISRN Applied Mathematics* 2013 (2013) 1–10. doi:10.1155/2013/567451.
- [21] M. B. Suleiman, H. Musa, F. Ismail, N. Senu, A new variable step size block backward differentiation formula for solving stiff initial value problems, *International Journal of Computer Mathematics* 90 (11) (2013) 2391–2408. doi:10.1080/00207160.2013.776677.
- [22] Z. B. Ibrahim, Block Backward Differentiation Formulas With Au-

- Automatic Order Selection For Solving Ordinary Differential Equations (2014) 7.
- [23] Z. B. Ibrahim, N. Zainuddin, K. I. Othman, M. Suleiman, I. S. Mohd Zawawi, Variable Order Block Method for Solving Second Order Ordinary Differential Equations, *Sains Malaysiana* 48 (8) (2019) 1761–1769. doi:10.17576/jsm-2019-4808-23.
- [24] K. Radhakrishnan, A. C. Hindmarsh, Description and Use of LSODE, the Livermore Solver for Ordinary Differential Equations, Tech. Rep. UCRL-ID-113855, Lawrence Livermore National Laboratory (1993).
- [25] H. Smith, Published on behalf of the International commission on Radiological Protection (1996) 224.
- [26] D. Pelowitz, MCNP – A General Monte Carlo N-Particle Transport Code, Version 6 – Volume 1 Overview and Theory, Tech. Rep. LA-CP-11-xxxx, Los Alamos National Laboratory (2011).
- [27] G. Firpo, M. Frignani, C. M. Viberti, Benchmarking of M AN C I N T A P 2.0, a parallel high-performance tool for neutron activation analysis in complex 4D scenarios, *The European Physical Journal Plus* 135 (1) (2020) 1–18. doi:10.1140/epjp/s13360-020-00162-9.
- [28] P. F. Rose, ENDF-201: ENDF/B-VI summary documentation, Tech. Rep. BNL-NCS-17541; ENDF-201, Brookhaven National Lab., Upton, NY (United States) (Oct. 1991). doi:10.2172/10132931.
- [29] M. B. Chadwick, P. Obložinský, M. Herman, N. M. Greene, R. D. McKnight, D. L. Smith, P. G. Young, R. E. MacFarlane, G. M. Hale, S. C. Frankle, A. C. Kahler, T. Kawano, R. C. Little, D. G. Madland, P. Moller, R. D. Mosteller, P. R. Page, P. Talou, H. Trellue, M. C. White, W. B. Wilson, R. Arcilla, C. L. Dunford, S. F. Mughabghab, B. Pritychenko, D. Rochman, A. A. Sonzogni, C. R. Lubitz, T. H. Trumbull, J. P. Weinman, D. A. Brown, D. E. Cullen, D. P. Heinrichs, D. P. McNabb, H. Derrien, M. E. Dunn, N. M. Larson, L. C. Leal, A. D. Carlson, R. C. Block, J. B. Briggs, E. T. Cheng, H. C. Huria, M. L. Zerkle, K. S. Kozier, A. Courcelle, V. Pronyaev, S. C. van der Marck, ENDF/B-VII.0: Next Generation Evaluated Nuclear Data Library for Nuclear Science and Technology, *Nuclear Data Sheets* 107 (12) (2006) 2931–3060. doi:10.1016/j.nds.2006.11.001.
- [30] Y. Kikuchi, M. of Jndc, Japanese Evaluated Nuclear Data Library, Version-3, JENDL-3, Nuclear Data for Science and Technology (1992) 793–799. doi:10.1007/978-3-642-58113-7_223.
- [31] M. B. Chadwick, M. Herman, P. Obložinský, M. E. Dunn, Y. Danon, A. C. Kahler, D. L. Smith, B. Pritychenko, G. Arbanas, R. Arcilla, R. Brewer, D. A. Brown, R. Capote, A. D. Carlson, Y. S. Cho, H. Derrien, K. Guber, G. M. Hale, S. Hoblit, S. Holloway, T. D. Johnson, T. Kawano, B. C. Kiedrowski, H. Kim, S. Kunieda, N. M. Larson, L. Leal, J. P. Lestone, R. C. Little, E. A. McCutchan, R. E. MacFarlane, M. MacInnes, C. M. Mattoon, R. D. McKnight, S. F. Mughabghab, G. P. A. Nobre, G. Palmiotti, A. Palumbo, M. T. Pigni, V. G. Pronyaev, R. O. Sayer, A. A. Sonzogni, N. C. Summers, P. Talou, I. J. Thompson, A. Trkov, R. L. Vogt, S. C. van der Marck, A. Wallner, M. C. White, D. Wiarda, P. G. Young, ENDF/B-VII.1 Nuclear Data for Science and Technology: Cross Sections, Covariances, Fission Product Yields and Decay Data, *Nuclear Data Sheets* 112 (12) (2011) 2887–2996. doi:10.1016/j.nds.2011.11.002.
- [32] A. J. Koning, D. Rochman, Modern Nuclear Data Evaluation with the TALYS Code System, *Nuclear Data Sheets* 113 (12) (2012) 2841–2934. doi:10.1016/j.nds.2012.11.002.

Highlights

RayActive: An all-in-one R2S neutron induced activation analysis tool based on new intrinsic resolution methods.

N. Dray, E. Suraud, C. Dossat, N. Chatry

- Neutron induced activation analysis is a complex and time consuming process
- RayActive is a CAD based neutron induced activation analysis prototype tool
- Inventory calculation is made with an internal 2 points Block BDF ODE solver
- RayActive is automated and as accurate as possible